INTERNATIONAL JOURNAL FOR NUMERICAL METHODS IN FLUIDS
Int. J. Numer. Meth. Fluids 2010; **62**:499–529
Published online 17 March 2009 in Wiley InterScience (www.interscience.wiley.com). DOI: 10.1002/fld.2032

An adaptive gradient smoothing method (GSM) for fluid dynamics problems

George X. Xu[1,*,†], G. R. Liu[2,3,‡] and Atusi Tani[4,‡]

[1]*Institute of High Performance Computing, Fusionopolis, 1 Fusionopolis Way, #16-16 Connexis, Singapore 138632, Singapore*
[2]*Centre for Advanced Computations in Engineering Science, Department of Mechanical Engineering, National University of Singapore, 10 Kent Ridge Crescent, Singapore 119260, Singapore*
[3]*Singapore-MIT Alliance (SMA), E4-04-10, 4 Engineering Drive 3, Singapore 117576, Singapore*
[4]*Department of Mathematics, Keio University, Hiyoshi, Kohoku-ku, Yokohama, Kanagawa 223-8522, Japan*

SUMMARY

In this paper, a novel adaptive gradient smoothing method (GSM) based on irregular cells and strong form of governing equations for fluid dynamics problems with arbitrary geometrical boundaries is presented. The spatial derivatives at a location of interest are consistently approximated by integrally averaging of gradients over a smoothing domain constructed around the location. Such a favorable GSM scheme corresponds to a compact stencil with positive coefficients of influence on regular cells. The error equidistribution strategy is adopted in the solution-based adaptive GSM procedure, and adaptive grids are attained with the remeshing techniques and the advancing front method. In this paper, the adaptive GSM has been tested for solutions to both Poisson and Euler equations. The sensitivity of the GSM to the irregularity of the grid is examined in the solutions to the Poisson equation. We also investigate the effects of error indicators based on the first derivatives and second derivatives of density, respectively, to the solutions to the shock flow over the NACA0012 airfoil. The adaptive GSM effectively yields much more accurate results than the non-adaptive GSM solver. The whole adaptive process is very stable and no spurious behaviors are observed in all testing cases. The cosmetic techniques for improving grid quality can effectively boost the accuracy of GSM solutions. It is also found that the adaptive GSM procedure using the second derivatives of density to estimate the error indicators can automatically and accurately resolve all key features occurring in the flow with discontinuities. Copyright © 2009 John Wiley & Sons, Ltd.

Received 21 May 2008; Revised 15 January 2009; Accepted 6 February 2009

KEY WORDS: numerical method; FVM; adaptive; fluid dynamics; GSM; GSD; stencil

*Correspondence to: George X. Xu, Institute of High Performance Computing, Fusionopolis, 1 Fusionopolis Way, #16-16 Connexis, Singapore 138632, Singapore.
†E-mail: xuxg@ihpc.a-star.edu.sg
‡Professor.

1. INTRODUCTION

In numerical methods, a gradient at a location is often approximated with the help of Taylor-series expansion or a predefined polynomial function [1]. Alternatively, it can also be approximated by spatial averaging of gradients over a smoothing domain constructed around the location of interest. Such a technique is referred as gradient smoothing operation [2].

The use of gradient smoothing operation can be found in many weak-form meshfree methods. It has been used by Chen *et al.* [3] for stabilizing the nodal integration in the Galerkin meshfree method. It is also used in the linearly conforming point interpolation method [4, 5] for solution stabilization and for obtaining upper bound solutions. In these methods, the gradient smoothing operation was used in the approximation of strains. With an adopted piecewise constant smoothing function, via Green–Gauss theorem (known as divergence theorem), the domain integration in the original form was converted into line integration along the boundaries of smoothing domain in two-dimensional problems. It was found that the stabilized nodal integration gave higher efficiency with desired accuracy and convergent properties. The use of smoothing operation also avoided the evaluation of derivatives of grid-free shape functions required by direct nodal integration and just resulted in higher accuracy. The smoothed gradient matrix was shown to satisfy linear exactness in the Galerkin approximation of a second-order partial differential equation. In addition, smoothing techniques have also been employed in the widely used smoothed particle method [6, 7] mainly as a general means of function approximation.

Most above-mentioned research efforts relate to the use of gradient smoothing operation for weak-form governing equations. In such applications, the gradient smoothing operation is only adopted as an auxiliary component in the development of main frameworks for various meshfree methods. A gradient smoothing method (GSM) for strong-form equations has been most recently developed [2], in which the gradient smoothing operation is consistently and successively used to approximate the first and second derivatives at different locations and the resultant instantaneous equations are solved subsequently. Various discretization schemes for approximating spatial derivatives have been devised and some favorable schemes valid for various types of grid are selected from the viewpoints of efficiency and accuracy. The excellent schemes for the GSM have been successfully formulated and applied for simulating compressible flows and heat conduction problems. Our previous efforts showed that the proposed GSM is conservative, conformal, efficient, robust, and accurate.

Our previous GSM solutions for heat conduction and compressible flow problems, as presented by Liu and Xu [2], have been attained using pre-generated fixed grids with nodes that can be irregularly distributed. Such fixed grids may not be good enough to cater for the flow phenomena involving abrupt changes, for example, a flow over an RAE2822 airfoil [2]. Noticeable discrepancy between GSM solution to the experimental data was still observed across the shock region, mainly due to the insufficiently fine cells in the shock area that is, in general, unknown when the grids are created before the analysis. Hence, it is very difficult to generate a good set of grid before the solutions to the flow field are attained. The solution-based adaptive processes [8, 9] give the solutions to overcome such a difficulty and consequently yield a set of optimal grid suitable for abrupt changes. The main objective in our current study is to develop an adaptive remeshing process for the robust, stable, and accurate GSM so as to automatically and successfully resolve the flows with abrupt changes, such as a shock flow, in a self-contained manner. Besides, the sensitivity of the GSM to the irregularity of grid is further examined.

DOI: 10.1002/fld

In this paper, our recent progress in the development of the adaptive GSM is presented. In the following sections, the principle of the GSM is first introduced. The GSM approximations to the gradients (first derivative) and the Laplace operator (second derivative) of a field variable are presented in detail. The adopted adaptive remeshing process using the advancing front technique is described in details. The adaptive GSM is then used to solve the Poisson equations for benchmarking purpose. The roles of some cosmetic postprocesses for adaptive grids, including removal of redundant triangles, diagonal swapping, and grid smoothing, are also addressed. Finally, the successful application of the adaptive GSM to resolve an actual fluid flow problem of an inviscid shock flow over the NANA0012 airfoil is presented.

2. GRADIENT SMOOTHING METHOD (GSM)

In the GSM, derivatives at various locations, such as at nodes, centroids of cells, and midpoints of cell-edges, are approximated using gradient smoothing operation over relevant gradient smoothing domains. This section briefly elucidates the fundamental principles and implementation procedure in the GSM.

2.1. Gradient smoothing operation

For simplicity, a two-dimensional problem is considered here to illustrate the gradient smoothing operation. Such a process was initially proposed to approximate a function or its gradient at a point [2, 6, 10, 11]. For example, the gradients of a field variable U at a point of interest at $\mathbf{x}_i$ in domain Ω_i can be approximated in the form of

$$\nabla U_i \equiv \nabla U(\mathbf{x}_i) \approx \int_{\Omega_i} \nabla U(\mathbf{x})\, \widehat{w}(\mathbf{x}-\mathbf{x}_i)\, \mathrm{d}\mathbf{x} \tag{1}$$

where ∇ is gradient operator and $\widehat{w}$ is a smoothing function.

If we integrate Equation (1) by parts or use divergence theorem, Equation (1) becomes

$$\nabla U_i \approx \oint_{\partial\Omega_i} U(\mathbf{x})\, \widehat{w}(\mathbf{x}-\mathbf{x}_i)\, \vec{n}\, \mathrm{d}s - \int_{\Omega_i} U(\mathbf{x}) \nabla \widehat{w}(\mathbf{x}-\mathbf{x}_i)\, \mathrm{d}V \tag{2}$$

where $\partial\Omega_i$ represents the boundary of the gradient smoothing domain and $\vec{n}$ denotes the outward-pointing unit normal vector on $\partial\Omega_i$, as shown in Figure 1.

The smoothing function, $\widehat{w}$, is chosen properly according to the requirement on the accuracy in approximation of the function, and needs to satisfy some conditions (see, for example, [2, 7]). For simplicity, the smoothing function in current study is set to be piecewise constant over the smoothing domain as follows:

$$\widehat{w} = \begin{cases} 1/V_i, & \mathbf{x} \in \Omega_i \\ 0, & \mathbf{x} \notin \Omega_i \end{cases} \tag{3}$$

where V_i stands for the area of the smoothing domain Ω_i. The proposed smoothing function can automatically satisfy the basic condition of partition of unity over the smoothing domain, e.g. $\int_{\Omega_i} \widehat{w}(\mathbf{x}-\mathbf{x}_i)\, \mathrm{d}V = 1$.

DOI: 10.1002/fld

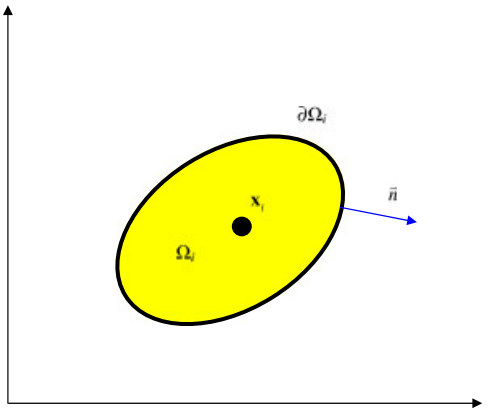

Figure 1. A smoothing domain for a point at $\mathbf{x}_i$.

Thus, the second term on the right-hand side in Equation (2) vanishes, and Equation (2) reduces to

$$\nabla U_i \approx \frac{1}{V_i} \oint_{\partial\Omega_i} U \vec{n} \, \mathrm{d}s \tag{4}$$

Equation (4) gives a simple way to approximate to gradients at a point by area-weighted integral along the boundary of a local smoothing domain. It is apparent that using Equation (4) is more efficient than using Equation (1) to approximate the gradients, because numerical integral along the boundary is much more cost-effective than over the surface of the smoothing domain.

Analogously, by successively applying the gradient smoothing technique for second-order derivatives [12–14], the Laplace operator at an arbitrary point $\mathbf{x}_i$ can be approximated as

$$\nabla \cdot (\nabla U_i) \approx \frac{1}{V_i} \oint_{\partial\Omega_i} \vec{n} \cdot \nabla U \, \mathrm{d}s \tag{5}$$

Hence, spatial derivatives at any point of interest can be approximated using Equations (4) and (5) over a smoothing domain that needs to be properly defined for a purpose [2].

2.2. Smoothing domains

In the GSM, the values of field functions are stored at nodes that can be irregularly distributed in space. By connecting nodes, the problem domain is first divided into a set of primitive cells of any shape. Because triangular cells can be automatically generated, they are usually preferred. Based on these cells, a smooth domain for any point of interest can be constructed. We devise different types of smoothing domains for approximating first derivative at different locations. Figure 2 shows three types of gradient smoothing domains, over which spatial derivatives are approximated with gradient smoothing operation. The first type of smoothing domain is the node-associated GSD (nGSD) for the approximation of derivatives at a node of interest. As shown in Figure 2, the nGSD is formed by connecting the centroids of relevant triangles with midpoints of influenced cell-edges. The second is identical to a primitive cell, which is used for approximating derivatives at the centroid of the cell, as in the cell-centered FVM [15]. It is called centroid-associated GSD

DOI: 10.1002/fld

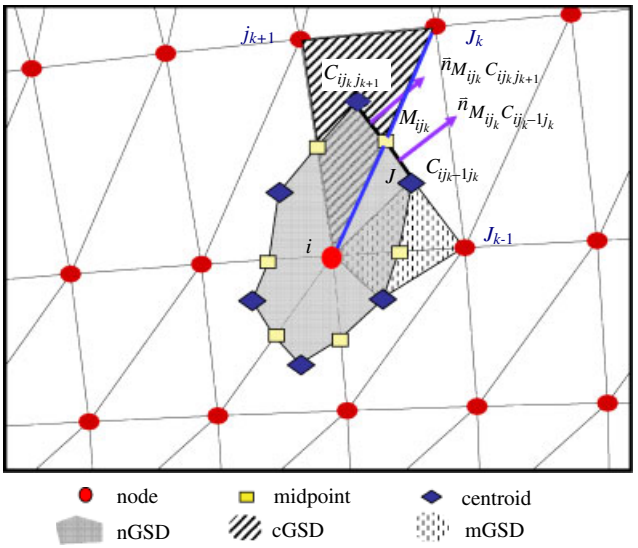

Figure 2. Illustration of gradient smoothing domains and domain-edge vectors adopted in GSM.

(cGSD) here. The third is named midpoint-associated GSD (mGSD) used for the calculation of the gradients at the midpoint of a cell-edge of interest. The proposed mGSD, as shown in Figure 2, is formed by connecting the end-nodes of the cell-edge with the centroids on the both sides of the cell-edge. As reported in [2], the adoption of gradient smoothing operation over such a mGSD to approximate the gradient at a midpoint, which is needed to discretized Equation (5), can successfully avoid the checkerboard problem that is usually encountered by the approximation based on simply arithmetic average of gradients at two constitute nodes. Furthermore, the resultant scheme is remarkably robust to the irregularity of triangular cells across the domain.

By virtue of Equations (4) and (5), spatial derivatives at any point of interest can be approximated based on the corresponding smoothing domain described above. As outlined by Liu and Xu [2], different schemes are devised and then evaluated on the basis of stencil analyses and numerical tests. As a result, a scheme which is based on one-point quadrature and consistent application of gradient smoothing at all locations of interest is most preferable, because of its balanced accuracy and computational efficiency, and attractive robustness to grid irregularity. In this paper, this scheme is adopted in the development of adaptive GSM.

2.3. Approximation to spatial derivatives

We now need to accurately predict the integrals along the boundaries of various types of GSDs. In this work, spatial derivatives (both first-order and second-order) at nodes are approximated using the one-point quadrature (rectangular rule). As such, the integrand (U or ∇U) for each domain-edge takes the values at the midpoint of the connected cell-edge. Such a procedure is independent of the values at centroids of cells and, therefore, the approximation for the gradients at centroids, which is necessarily needed in two-point quadrature schemes (see, for example, [5]), is avoided. Two-point quadrature is only used for the approximation of gradients at midpoints of cell-edges. Details will be elucidated below.

DOI: 10.1002/fld

2.3.1. First derivatives at nodes. With the gradient smoothing operation using Equation (4), the first-order derivatives at nodes can be approximated as

$$\frac{\partial}{\partial x}(U_N)_i \approx \frac{1}{(V_N)_i}\sum_{k=1}^{n_i}(\Delta S_N^x)_{ij_k}(U_M)_{ij_k} \tag{6}$$

$$\frac{\partial}{\partial y}(U_N)_i \approx \frac{1}{(V_N)_i}\sum_{k=1}^{n_i}(\Delta S_N^y)_{ij_k}(U_M)_{ij_k} \tag{7}$$

where

$$(\Delta S_N^x)_{ij_k} = \Delta S_{M_{ij_k}C_{ij_kj_{k+1}}}(n_x)_{M_{ij_k}C_{ij_kj_{k+1}}} + \Delta S_{M_{ij_k}C_{ij_{k-1}j_k}}(n_x)_{M_{ij_k}C_{ij_{k-1}j_k}} \tag{8}$$

$$(\Delta S_N^y)_{ij_k} = \Delta S_{M_{ij_k}C_{ij_kj_{k+1}}}(n_y)_{M_{ij_k}C_{ij_kj_{k+1}}} + \Delta S_{M_{ij_k}C_{ij_{k-1}j_k}}(n_y)_{M_{ij_k}C_{ij_{k-1}j_k}} \tag{9}$$

Here, i denotes the node of interest and j_k is the other end-node of the cell-edge linked to node i (see Figure 2). M_{ij_k} denotes the midpoint of the cell-edge of interest, ij_k. $C_{ij_kj_{k+1}}$ and $C_{ij_{k-1}j_k}$ represent the centroids of two triangular cells connected to the cell-edge ij_k. The total number of supporting nodes within the stencil of the node i is denoted by n_i. U_N, U_M, and U_C denote values of the field variable at nodes, midpoints of cell-edges, and centroids of triangular cells, respectively. Thanks to the one-point quadrature, for an nGSD of interest, a pair of domain-edges connected with cell-edge ij_k are evaluated in a lumped manner. ΔS_N^x and ΔS_N^y correspond to the two components of the paired domain-edges. n_x and n_y represent the two components of the unit normal vector of the domain-edge under a Cartesian coordinate system. V_N is the area of an nGSD. These geometrical parameters are calculated and stored before the resultant algebraic equations are solved.

The values of the field variable U at non-storage locations, i.e. at midpoints and centroids, are computed by simple interpolation of function values at related nodes, respectively, in the manner of

$$(U_M)_{ij_k} = \frac{(U_N)_i + (U_N)_{j_k}}{2} \tag{10}$$

$$(U_C)_{ij_kj_{k+1}} = \begin{cases} \dfrac{(U_N)_i + (U_N)_{j_k} + (U_N)_{j_{k+1}}}{3}, & 1 \leqslant k < n_i \\ \dfrac{(U_N)_i + (U_N)_{j_{n_i}} + (U_N)_{j_1}}{3}, & k = n_i \end{cases} \tag{11}$$

$$(U_C)_{ij_{k-1}j_k} = \begin{cases} \dfrac{(U_N)_i + (U_N)_{j_k} + (U_N)_{j_{k-1}}}{3}, & 1 < k \leqslant n_i \\ \dfrac{(U_N)_i + (U_N)_{j_1} + (U_N)_{j_{n_i}}}{3}, & k = 1 \end{cases} \tag{12}$$

The values of field function at centroids are only needed for approximation of gradients at midpoints of cell-edges.

DOI: 10.1002/fld

2.3.2. Second derivatives at nodes. In the GSM, with one-point quadrature, the second derivatives in Laplace operator are approximated using Equation (5) in the following manner:

$$\nabla\cdot(\nabla U_N)_i \approx \frac{1}{\Omega_i}\sum_{k=1}^{n_i}\left[\frac{\partial}{\partial x}(U_M)_{ij_k}(\Delta S_N^x)_{ij_k}+\frac{\partial}{\partial y}(U_M)_{ij_k}(\Delta S_N^y)_{ij_k}\right] \tag{13}$$

It is apparent that the gradients at midpoints are needed to complete the approximation of second-order derivatives at nodes. As mentioned in the previous section, the two-point quadrature is proposed to approximate gradients at midpoints in the GSM. As a result, using Equation (4) over the relevant mGSD as shown in Figure 2, the first-order derivatives at the midpoint of cell-edge of interest, ij_k, are attained by

$$\begin{aligned}\frac{\partial}{\partial x}(U_M)_{ij_k} \approx \Bigg\{&\frac{1}{2}(\Delta S_M^x)_{iC_{ij_kj_{k+1}}}[(U_N)_i+(U_C)_{ij_kj_{k+1}}]+\frac{1}{2}(\Delta S_M^x)_{j_kC_{ij_kj_{k+1}}}[(U_N)_{j_k}+(U_C)_{ij_kj_{k+1}}]\\&+\frac{1}{2}(\Delta S_M^x)_{iC_{ij_{k-1}j_k}}[(U_N)_i+(U_C)_{ij_{k-1}j_k}]+\frac{1}{2}(\Delta S_M^x)_{j_kC_{ij_{k-1}j_k}}[(U_N)_{j_k}+(U_C)_{ij_{k-1}j_k}]\Bigg\}\\&\times\frac{1}{(V_M)_{ij_k}}\end{aligned} \tag{14}$$

$$\begin{aligned}\frac{\partial}{\partial y}(U_M)_{ij_k} \approx \Bigg\{&\frac{1}{2}(\Delta S_M^y)_{iC_{ij_kj_{k+1}}}[(U_N)_i+(U_C)_{ij_kj_{k+1}}]+\frac{1}{2}(\Delta S_M^y)_{j_kC_{ij_kj_{k+1}}}[(U_N)_{j_k}+(U_C)_{ij_kj_{k+1}}]\\&+\frac{1}{2}(\Delta S_M^y)_{iC_{ij_{k-1}j_k}}[(U_N)_i+(U_C)_{ij_{k-1}j_k}]+\frac{1}{2}(\Delta S_M^y)_{j_kC_{ij_{k-1}j_k}}[(U_N)_{j_k}+(U_C)_{ij_{k-1}j_k}]\Bigg\}\\&\times\frac{1}{(V_M)_{ij_k}}\end{aligned} \tag{15}$$

where V_M represents the area of an mGSD. The relevant domain-edge vectors, ΔS_M^x and ΔS_M^y, for the mGSD of interest, are calculated as follows:

$$\begin{aligned}(\Delta S_M^x)_{iC_{ij_kj_{k+1}}}&=\Delta S_{iC_{ij_kj_{k+1}}}(n_x)_{iC_{ij_kj_{k+1}}},\quad (\Delta S_M^y)_{iC_{ij_kj_{k+1}}}=\Delta S_{iC_{ij_kj_{k+1}}}(n_y)_{iC_{ij_kj_{k+1}}}\\(\Delta S_M^x)_{j_kC_{ij_kj_{k+1}}}&=\Delta S_{j_kC_{ij_kj_{k+1}}}(n_x)_{j_kC_{ij_kj_{k+1}}},\quad (\Delta S_M^y)_{j_kC_{ij_kj_{k+1}}}=\Delta S_{j_kC_{ij_kj_{k+1}}}(n_y)_{j_kC_{ij_kj_{k+1}}}\end{aligned} \tag{16}$$

$$\begin{aligned}(\Delta S_M^x)_{iC_{ij_{k-1}j_k}}&=\Delta S_{iC_{ij_{k-1}j_k}}(n_x)_{iC_{ij_{k-1}j_k}},\quad (\Delta S_M^y)_{iC_{ij_{k-1}j_k}}=\Delta S_{iC_{ij_{k-1}j_k}}(n_y)_{iC_{ij_{k-1}j_k}}\\(\Delta S_M^x)_{j_kC_{ij_{k-1}j}}&=\Delta S_{j_kC_{ij_{k-1}j_k}}(n_x)_{j_kC_{ij_{k-1}j_k}},\quad (\Delta S_M^y)_{j_kC_{ij_{k-1}j}}=\Delta S_{j_kC_{ij_{k-1}j_k}}(n_y)_{j_kC_{ij_{k-1}j_k}}\end{aligned} \tag{17}$$

For regular grids (cells in square and equilateral triangle shapes), the compact stencils with positive weighting coefficients for the approximated Laplace operator are obtained, as shown in Figure 3. As addressed in the stencil analyses in [2], such a scheme corresponds to second-order accuracy and the involved computation is cost-effective. This is one of the reasons why such a discretization scheme for spatial derivatives is promoted.

It should be mentioned that the principle about gradient smoothing operation can be extended easily for three-dimensional problems. For example, in cases where tetrahedral elements are used as

DOI: 10.1002/fld

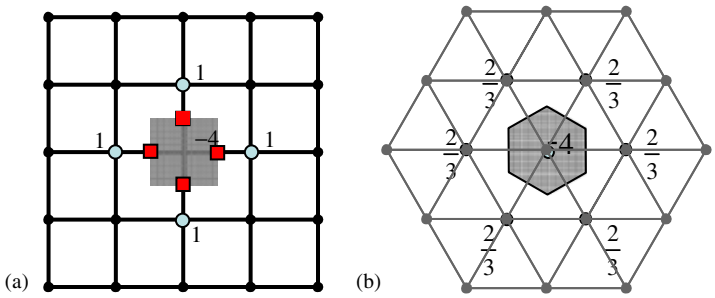

Figure 3. Stencils for the approximation of the Laplace operator: (a) square and (b) equilateral triangles.

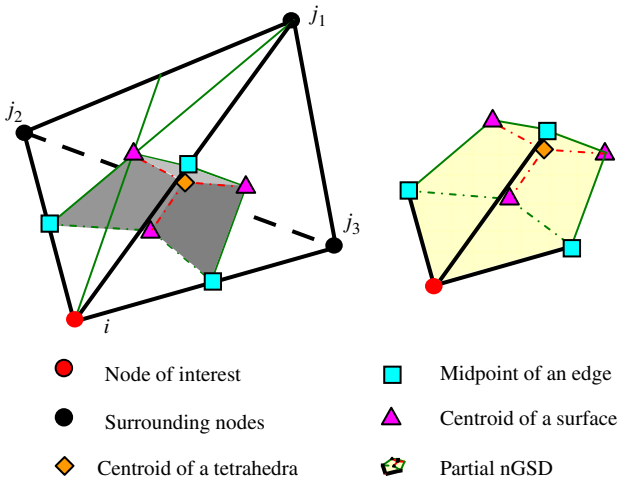

Figure 4. Partially formed three-dimensional node-associated gradient smoothing domain based on a tetrahedral primal element.

primal elements, a typical node-associated smoothing domain can be formed by joining all domain faces each of which is generated by connecting the midpoint of a common edge, the centroids of two involved element surfaces and the centroid of the involved primal element. A partially formed three-dimensional node-associated gradient smoothing domain based on a tetrahedral primal element is shown in Figure 4, where the relevant domain faces are shaded. Hence, the boundary integrals occurring in Equations (4) and (5) would be replaced by integrals over domain surfaces of such a three-dimensional nGSD. Accordingly, in three-dimensional applications, the surface normals should be used instead of boundary normals for three-dimensional problems.

2.4. Approximation to temporal derivatives

For a transient or pseudo-transient problem, the governing equation can be rewritten in the form of

$$\frac{\partial}{\partial t}(U_N) = -R \tag{18}$$

DOI: 10.1002/fld

where R represents the residual dependent of the field variable U and its derivatives. In current study, the temporal term $(\partial U_N/\partial t)$ is approximated with the following explicit five-stage Runge–Kutta (*RK*5) method [16]:

$$\begin{aligned}
(U_N)_i^{(0)} &= (U_N)_i^n \\
(U_N)_i^{(1)} &= (U_N)_i^{(0)} - \alpha_1 \Delta t\, R_i^{(0)} \\
(U_N)_i^{(2)} &= (U_N)_i^{(0)} - \alpha_2 \Delta t\, R_i^{(1)} \\
(U_N)_i^{(3)} &= (U_N)_i^{(0)} - \alpha_3 \Delta t\, R_i^{(2)} \\
(U_N)_i^{(4)} &= (U_N)_i^{(0)} - \alpha_4 \Delta t\, R_i^{(3)} \\
(U_N)_i^{(5)} &= (U_N)_i^{(0)} - \alpha_5 \Delta t\, R_i^{(4)}
\end{aligned} \tag{19}$$

where the residual $R_i^{(k)}$ is evaluated with the values of the field function and its derivatives approximated with the kth-stage *RK* solution at node i for every time-step. Δt denotes the time-step, and the coefficients adopted in current study are $\alpha_1 = 0.0695$, $\alpha_2 = 0.1602$, $\alpha_3 = 0.2898$, $\alpha_4 = 0.5060$, and $\alpha_5 = 1.000$.

The *RK5* method has been widely used in the simulations of many transient fluid flow problems, because of its satisfactory efficiency and stability. Besides, with the *RK5* method, only the 0th- and 5th-stage solutions at nodes are needed to be stored in memory, which saves a lot in computational demands.

3. ADAPTIVE REMESHING TECHNIQUE

The adaptive process aims at yielding a set of 'optimal' grid on which an anticipated accuracy can be achieved. Such a grid, as outlined by Babuska and Rheinboldt [17], corresponds to equally distributed errors across the field. This implies that the 'optimal' grid can be achieved with the help of the heuristic error equidistribution strategy. Thus, in current study, an adaptive process based on the error equidistribution strategy is developed and used to boost the GSM solver for better accuracy. In the proposed adaptive process, a directional error indicator at each node for a current grid is evaluated first, followed by the determination of meshing parameters based on error equidistribution strategy. Once the meshing parameters are obtained, the whole field will be remeshed with the advancing front technique. The whole process is carried out in an iterative way till the expected accuracy or number of adaptive loops is reached. This section contributes to the brief introduction about the directional error indicator, at length explanation how to determine the meshing parameters required by the advancing front technique, and the description of the overall adaptive GSM procedure.

3.1. Directional error indicator

In an adaptive process, it is desirable to choose an appropriate error indicator which can be used to identify the regions for further either refinement or coarsening. The direction-oriented error indicator as outlined by Peiro *et al.* [18] cannot only serve such a purpose but assist to determine the coordinates of nodes for a new set of grid across the field. Therefore, it is adopted in the current

DOI: 10.1002/fld

study. For example, in a one-dimensional problem, using finite element method procedure, the variation of the error E within a cell in which the interested point x is located can be expressed as

$$E_e = \frac{1}{2}\xi(h-\xi)\left|\frac{\mathrm{d}^2U}{\mathrm{d}x^2}\right| \tag{20}$$

where ξ and h, respectively, denote a local cell coordinate and the cell length. This relates the error with the cell length and the second derivative at point x.

Furthermore, the root mean-square error over the cell can be computed as

$$\|E_e\|_{L_2} = \sqrt{\int_0^h \frac{E_e^2}{h}\,\mathrm{d}U} = \frac{1}{\sqrt{120}}h^2\left|\frac{\mathrm{d}^2U}{\mathrm{d}x^2}\right| \tag{21}$$

According to error equidistribution strategy, a set of 'optimal grid' corresponds to the case where the errors are equally distributed across the field, implying that

$$h^2\left|\frac{\mathrm{d}^2U}{\mathrm{d}x^2}\right| = C \tag{22}$$

where C is a positive constant.

More precisely, if δ is used to denote the 'optimal' spacing, for the set of 'optimal' grid, the following relation holds:

$$\delta^2\left|\frac{\mathrm{d}^2U}{\mathrm{d}x^2}\right| = C \tag{23}$$

This equation gives the way to determine the 'optimal' spacing on conditions that the second derivatives on a current set of one-dimensional grid are approximated.

Equation (23) can be directly extended to multi-dimensional problems. For a 2D problem as concerned here, it can be written in the quadratic form as

$$\delta_\alpha^2\left(\sum_{i,j=1}^{2} m_{ij}\alpha_i\alpha_j\right) = C \tag{24}$$

where α is an arbitrary unit vector, δ_α is the spacing along the direction of α, and m_{ij} are the components of a 2×2 symmetric matrix of second derivatives, which is

$$m_{ij} = \frac{\partial^2 U_N}{\partial x_i \partial x_j} \tag{25}$$

The meaning of Equation (24) is graphically illustrated in Figure 5 which shows how the values of the spacing in the α direction can be obtained as the distance from the origin to the point of intersection of the vector α with the boundary of an ellipse. The major and minor axial directions (α_1 and α_2), and the lengths of semimajor and semiminor axes (δ_1 and δ_2) for the ellipse can be readily computed, once the eigenvalues and eigenvectors of the matrix $\mathbf{m}$ are obtained, which will be shown in the following section.

As shown in Equation (25), the second derivatives are required to be evaluated for estimating numerical errors. Alternatively, Giraldo [19] has used the first derivatives for adaptive solutions

DOI: 10.1002/fld

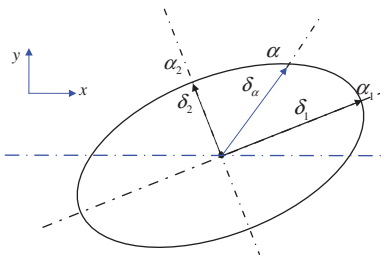

Figure 5. Determination of nodal spacing δ along a direction α.

to fluid dynamic problems, for their obvious physical meanings. In doing so, the gradients that are necessarily approximated in solution process are directly used in the error estimation. This becomes particularly attractive for inviscid flows, since there are no second derivatives at all appearing in original governing equations. Hence, the proposed variation is much more cost effective. Accordingly, the components of modified matrix **m** become

$$m_{ij} = \frac{\partial U_N}{\partial x_i} \frac{\partial U_N}{\partial x_j} \tag{26}$$

In current study, the both options for approximating matrix **m** are examined in testing cases. Some interesting results will be discussed in the section about numerical examples.

It should be pointed out that the attained grid is almost optimal when the local errors are approximately equal at all nodes. Therefore, this approach described above is an asymptotic method and demands iterative operation. However, as addressed by Peiro *et al.* [18], though these error indicators have no rigorous mathematical proof, considerable success has been achieved with their use in practical situations [8].

In addition, the presented error indicator is direction oriented so that it can be used to generated anisotropic grid by taking account of direction-dependent flow phenomena, such as shocks, contact discontinuities, etc. Such features can be most economically represented on grids which are stretched in appropriate directions. Besides, we have interests in the potential applications for problems pertaining to moving objects and fluid–structure interactions. In such cases, large changes in geometries and relative locations may occur, which sometimes violate the use of local treatment techniques including node motion and local enrichment. Comparatively, the present remeshing technique has its distinct advantages for such types of applications [20]. In present study, we restrict our interest only to isotropic grid for the fixed computational domain. Our continuous efforts will be rendered to explore the adaptive strategy with anisotropic grid based on such a directional error indicator for time-dependent computational domains.

Although we restrict our focus on two-dimensional application in current study, the approach described above can be extended for three-dimensional problems in a straightforward way.

3.2. Meshing parameters

Once the first derivatives are approximated based on the current grid and a value for constant C is specified, Equation (24) with respect to 'optimal' spacing and nodal directions can be solved. In the proposed adaptive process, three grid parameters for each node, i.e. the node spacing (δ) equal to the length of the semiminor axis, the stretching ratio (s) and the stretching direction (α) along

DOI: 10.1002/fld

the major axis, are used for grid regeneration. Based on a set of current grid and a user-specified value for constant C, these parameters can be computed as

$$\delta = \delta_2 = \sqrt{\frac{C}{\lambda_2}} \tag{27}$$

$$s = \frac{\delta_1}{\delta_2} = \sqrt{\frac{\lambda_2}{\lambda_1}} \tag{28}$$

$$\alpha = \alpha_1 \tag{29}$$

where λ_1 and λ_2 denote the eigenvalues of the matrix $\mathbf{m}$ at a node, respectively. Since major and minor axes are orthogonal with each other, the major axis direction, α_1, is calculated and chosen as one of the grid parameters. It can be determined with the eigenvectors for the matrix $\mathbf{m}$.

In order to generate a set of reasonable grid, two threshold values ($\delta_{\min}$ and $\delta_{\max}$) are specified as the bounds for the commutated spacing resulting from Equation (27) such that $\delta_{\min} \leqslant \delta \leqslant \delta_{\max}$. The maximum value $\delta_{\max}$ is mainly used to avoid meaninglessly large spacing due to a vanishing eigenvalue in Equation (27). The value of $\delta_{\max}$ is usually chosen as the cell spacing adopted in regions with uniform flow behaviors. The minimum value $\delta_{\min}$ is used for preventing the algorithm from creating an excessive refinement of cells in regions with large gradients, such as in shock region. Besides, since we are interested in the isotropic grid in current study, the stretching ratio is fixed at 1.0 throughout the numerical examples presented in this paper.

It is clear that the grid parameters for new grid generation depend strongly upon the choice of the constant, C. In the present practice, it is defined as

$$C = \lambda_{\max} \delta_{\min} \tag{30}$$

where $\lambda_{\max}$ is the maximum eigenvalue in the entire domain.

Once the grid parameters are determined as described above, the adaptive grid can be regenerated with the advanced front technique [9] which will be described in the following section.

3.3. Advancing front technique

The advancing front technique has a distinctive feature that cells and points are generated simultaneously. This enables the generation of cells of variable size and stretching, and differs from the Delaunay concepts [20] which usually connect the nodes that are already distributed in space. In general, the advancing front technique can result in high quality grids, and also offers the flexibility in generating anisotropic grid and the liability in handling moving components. For the sake of continuous studies to some broad extents, this technique is adopted in the development of adaptive GSM.

In general, the advancing front technique is a bottom-up approach for grid generation. Firstly, each boundary curve is discretized in turn. Nodes are placed on the boundary curve components and then contiguous nodes are joined with straight line segments. These segments will become edges of triangular cells in the later stage. The length of these segments must, therefore, be consistent with the desired local distribution of grid spacings which are computed as described in the preceding section. Successively, the triangular cells are generated. For a two-dimensional domain, all the sides produced in the first step are assembled as initial front. At any given time, the

DOI: 10.1002/fld

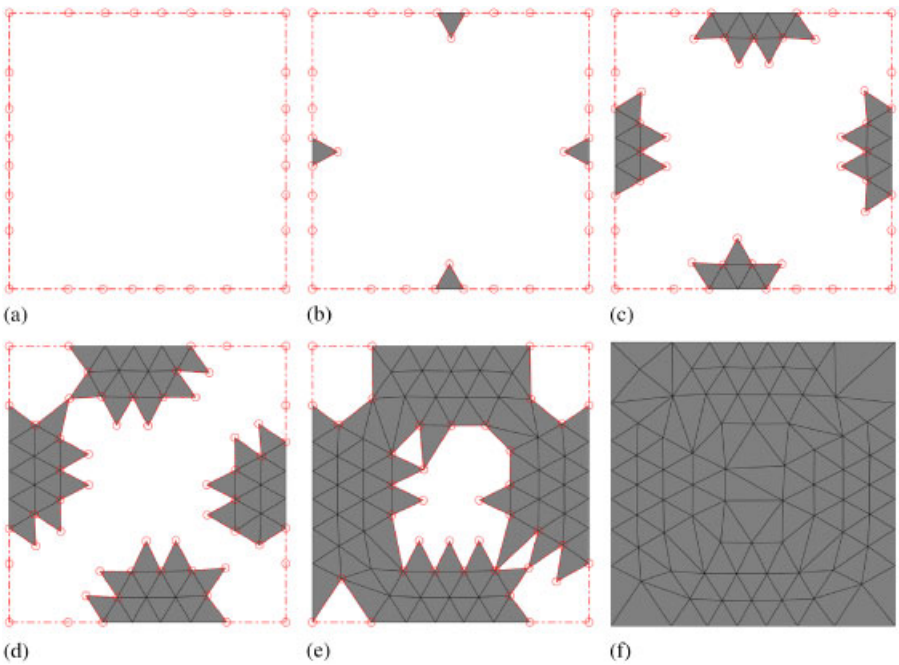

Figure 6. Triangulation process used in our adaptive GSM code based on advancing front technique.

front contains the set of all the sides which are currently available to form a triangular cell. Thus, the front is a dynamic data structure which is updated continuously during the generation process. A side is selected from the front and a triangular element is generated according to computed grid parameters. The triangulation process may involve creating a new node or simply connecting the side to an existing node. Once the triangle is formed, the front is updated by removing the old side out of the front list and adding the new sides into the front list. Then the triangulation proceeds until the contents in the front become empty. Figure 6 illustrates the grid generation process with the advancing front technique for a square planar domain where the initial front and the form of the grid at various stages are depicted.

In-depth description about the advancing front technique can be found in [20].

3.4. The adaptive GSM procedure

The overall adaptive GSM solution procedure is summarized as follows:

Step 1: GSM solutions including first-order derivatives are approximated according to a set of initial grid.

Step 2: The grid parameters (δ, s and α) across the whole computational domain are calculated based on the current grid.

Step 3: Discretization of boundary curves is performed using grid parameters obtained in Step 2. The discretized boundaries are used as the initial fronts for the advancing front method.

Step 4: The triangulation process is carried out with the advancing front technique using the grid parameters attained in Step 2, so as to generate the new adaptive grid.

DOI: 10.1002/fld

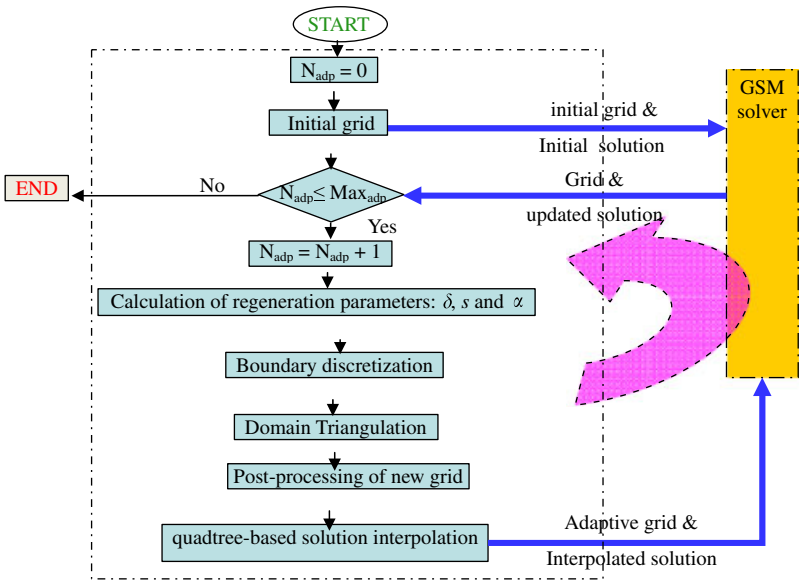

Figure 7. Workflow of the overall adaptive procedure adopted in the adaptive GSM.

Step 5: Cosmetic techniques including diagonal swapping, removal of worse cells and grid smoothing are applied to the new set of grid for the sake of improving grid quality.

Step 6: Interpolate the GSM solution for the current grid onto the new adaptive grid with the help of quad-tree searching technique.

Step 7: Compute the solutions with GSM solver based on the new set of adaptive grid and interpolated solutions obtained in Step 6.

Step 8: Repeat from Step 2 to Step 7, till the expected accuracy or the maximum number of adaptive cycles is achieved.

The workflow of the overall adaptive GSM procedure as described above is shown in Figure 7.

During the adaptive process, a background grid for a problem of interest is needed mainly for geometry definition. It is defined in a file with contents about the nodes composed of the background grid, boundary segments, and supporting curves. For a simple problem as a square domain, two cells are sufficient as the background grid. If a curve boundary exists in the problem of interest, a sufficiently large number of nodes are required for accurately representing the shape of the boundary. The file for the background grid is never altered during the adaptive process.

An initial grid with full meshing information for a problem of interest is required at the very beginning of the adaptive process. Usually, the initial grid is very coarse consisting only of a small number of triangles that can be manually defined. Such an initial grid can be replaced by a set of well-defined grid, if available. The initial grid will be used for attaining the first set of solution in the use of GSM solver. After that, it will be repeated replaced by the resultant 'optimal' grid as the adaptive process advances.

Some post-processes aiming at improving quality of new grid, including removal of undesirable cells, diagonal swapping, and grid smoothing, are carried out right after each set of new grid is generated with the advancing front technique. The undesirable triangular cells are not necessarily

DOI: 10.1002/fld

bad in terms of quality but may be redundant. The removal of those cells can favorably result in the reduction in the number of cells and nodes. The diagonal swapping is achieved by simply reconnecting the existing nodes locally so that the grid is optimized. The existing nodes and the number of cells will not be changed during such a process. In the adopted grid smoothing process, an interior node of the grid is shifted towards the centroid of the polygon formed by its neighboring cells. As a result, the grid quality can be improved in a more isotropic manner. The essence and effects of these cosmetic techniques will be addressed in details in the numerical testing cases.

At the end of each adaptive cycle, the interpolation of GSM solutions from the current grid onto a set of adaptive grid is performed. Initially, for each node in the set of new grid, the cell that contains the node of interest is first needed to be found. The searching procedure is facilitated to great extents with the use of quad-tree searching algorithm [21]. The quad-tree data structure for each set of current grid has been well defined before the generation of new grid. It is also used for the interpolation of grid parameters from the current grid to any newly created node in the processes of boundary discretization and domain triangulation. Subsequently, the interpolation is carried out using weak Lagrange–Galerkin procedure [19]. The interpolated solutions will be used as the initial solutions for the consequent GSM computation.

4. NUMERICAL EXAMPLES

Numerical tests on two-dimensional Poisson and Euler equations are conducted using our adaptive GSM code as described above.

4.1. Solutions to Poisson equations

4.1.1. Governing equations. Poisson equation for a square computational domain is first solved with our GSM code. The Poisson equation governs many physical problems, such as the heat conduction problems with sources. In current study, the Dirichlet conditions are prescribed on all boundaries. The pseudo-transient approach is adopted for pursuing steady-state solutions.

The governing equations under investigation take the following form:

$$\frac{\partial U}{\partial t}=\frac{\partial^2 U}{\partial x^2}+\frac{\partial^2 U}{\partial y^2}-f(x,y) \quad (0\leqslant x\leqslant 1, 0\leqslant y\leqslant 1) \tag{31}$$

The source, initial conditions, and analytical solution are given as follows:

$$\begin{aligned} &f(x,y,t)=\sin(\pi x)\sin(\pi y)\\ &U(x,y,0)=0 \end{aligned} \quad (0\leqslant x\leqslant 1, 0\leqslant y\leqslant 1) \tag{32}$$

$$\hat{U}(x,y)=-\frac{1}{2\pi^2}\sin(\pi x)\sin(\pi y) \quad (0\leqslant x\leqslant 1, 0\leqslant y\leqslant 1) \tag{33}$$

The contour plots of the analytical solution to the problem and the magnitude of its gradients are shown in Figure 8(a)–(b).

As shown in Figure 8(b), the red spots represent the regions with larger gradients, while blue spots indicate the regions with smaller gradients. We expect to see more nodes deployed in the red spots and fewer nodes in the blue areas, when the proposed adaptive process is engaged to remesh the domain.

DOI: 10.1002/fld

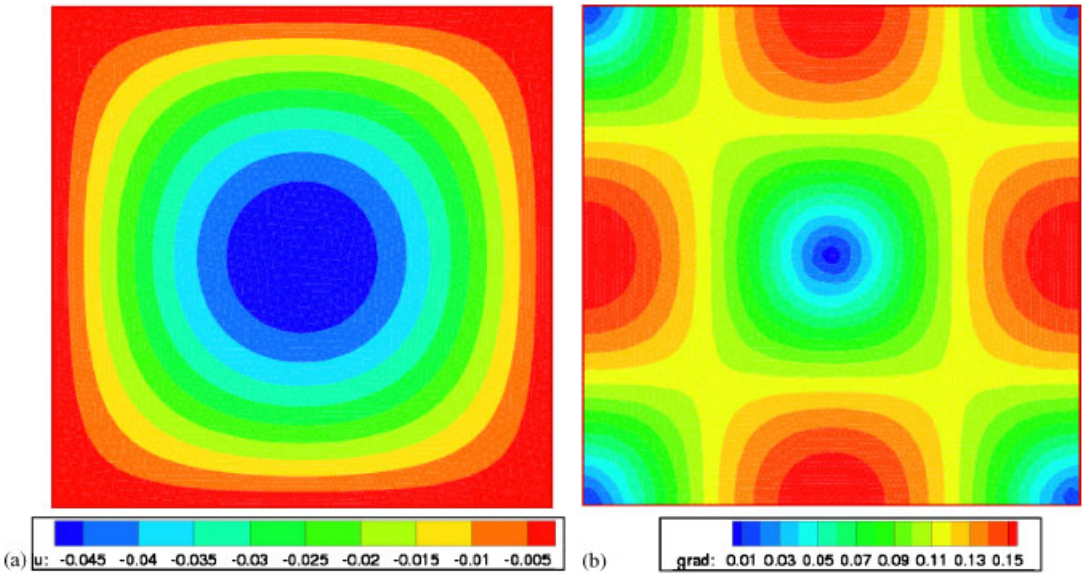

Figure 8. Contour plots of analytical solutions to the Poisson problem: (a) field function and (b) magnitude of resultant gradients.

4.1.2. Evaluation of numerical errors. Three types of numerical errors are evaluated in the study. The convergence error index, ε_{con}, takes the form of

$$\varepsilon_{\text{con}} = \sqrt{\sum_{i=1}^{n_{\text{node}}} (U_i^{(n+1)} - U_i^{(n)})^2} \Bigg/ \sqrt{\sum_{i=1}^{n_{\text{node}}} (U_i^{(1)} - U_i^{(0)})^2} \tag{34}$$

where $U_i^{(n)}$ denotes the predicted value of the field variable at node i at the nth iteration, and n_{node} is the total number of nodes in the domain. The value of ε_{con} is monitored during iterations and used to terminate the iterative process. In most simulations, in order to exclude the effect due to the temporal discretization, computations are not stopped until ε_{con} becomes stabilized, as indicated in Figure 9.

The numerical error in a GSM solution for the overall field is defined using L_2-norm of error, in the manner of

$$\text{error} = \sqrt{\sum_{i=1}^{n_{\text{node}}} (U_i - \hat{U}_i)^2} \Bigg/ \sqrt{\sum_{i=1}^{n_{\text{node}}} \hat{U}_i^2} \tag{35}$$

where U_i and $\hat{U}_i$ are predicted and analytical solutions at node i, respectively. This type of error is used to compare the accuracy among different schemes.

The third type of error is the node-wise relative error, which is estimated in the form of

$$\text{rerror}_i = |U_i - \hat{U}_i| / |\hat{U}_i| \tag{36}$$

The node-wise relative errors distributed over the computational domain are used to identify problematic regions in simulations.

DOI: 10.1002/fld

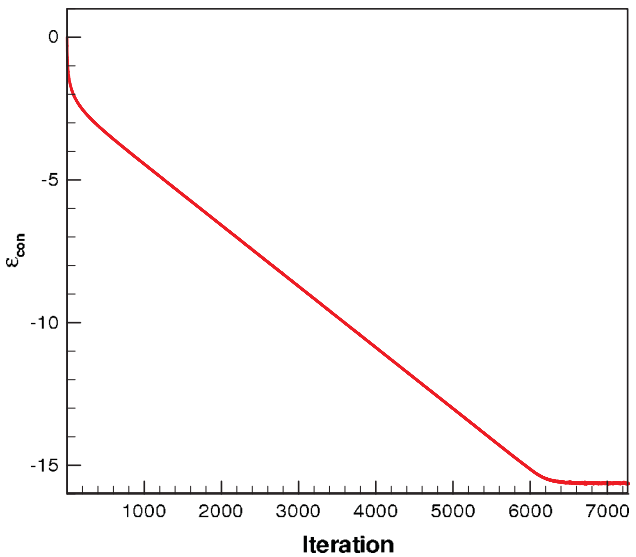

Figure 9. Plot of the profile on convergence history.

4.1.3. Adaptive solutions. In this study, we find that the controlled advancing front technique may result in irregular triangles with bad quality. The irregularity of all triangular cells in the computational domain can be quantified with the following formula:

$$\gamma = \frac{\sum_{i=1}^{n_e} \dfrac{(a_i - b_i)^2 + (b_i - c_i)^2 + (c_i - a_i)^2}{a_i^2 + b_i^2 + c_i^2}}{n_e} \tag{37}$$

where a_i, b_i, and c_i, respectively, denote the lengths of cell-edges of a triangular cell, and n_e stands for the total number of cells in the overall domain. Equation (37) is derived from the formula proposed by Stillinger *et al.* [22] for a single triangle. According to Equation (37), the irregularity vanishes for equilateral triangles and positive for all other shapes including isosceles triangles. The bigger the value of γ, the more irregular the grid.

Besides, as indicated by Liu [23], the average nodal spacing, h, for a set of irregular triangular grid may be estimated as

$$h = \frac{V}{\sqrt{n_{\text{node}} - 1}} \tag{38}$$

where V and n_{node} denote the area of the overall computational domain and the total number of nodes across the domain, respectively. It is apparent that the averaged nodal spacing decreases as the number of nodes increases.

The consequent adaptive grids for the Poisson problem, which are attained with the proposed adaptive remeshing procedure, are shown in Figure 10(a)–(e). The relatively uniform grid, as shown in Figure 10(a), is chosen as the initial grid on which the GSM solution is initially pursued. The grid parameters are then computed according to the equidistribution criterion as outlined in the previous section. For each adaptive remeshing procedure, the threshold value of $\delta_{\min}$ is

DOI: 10.1002/fld

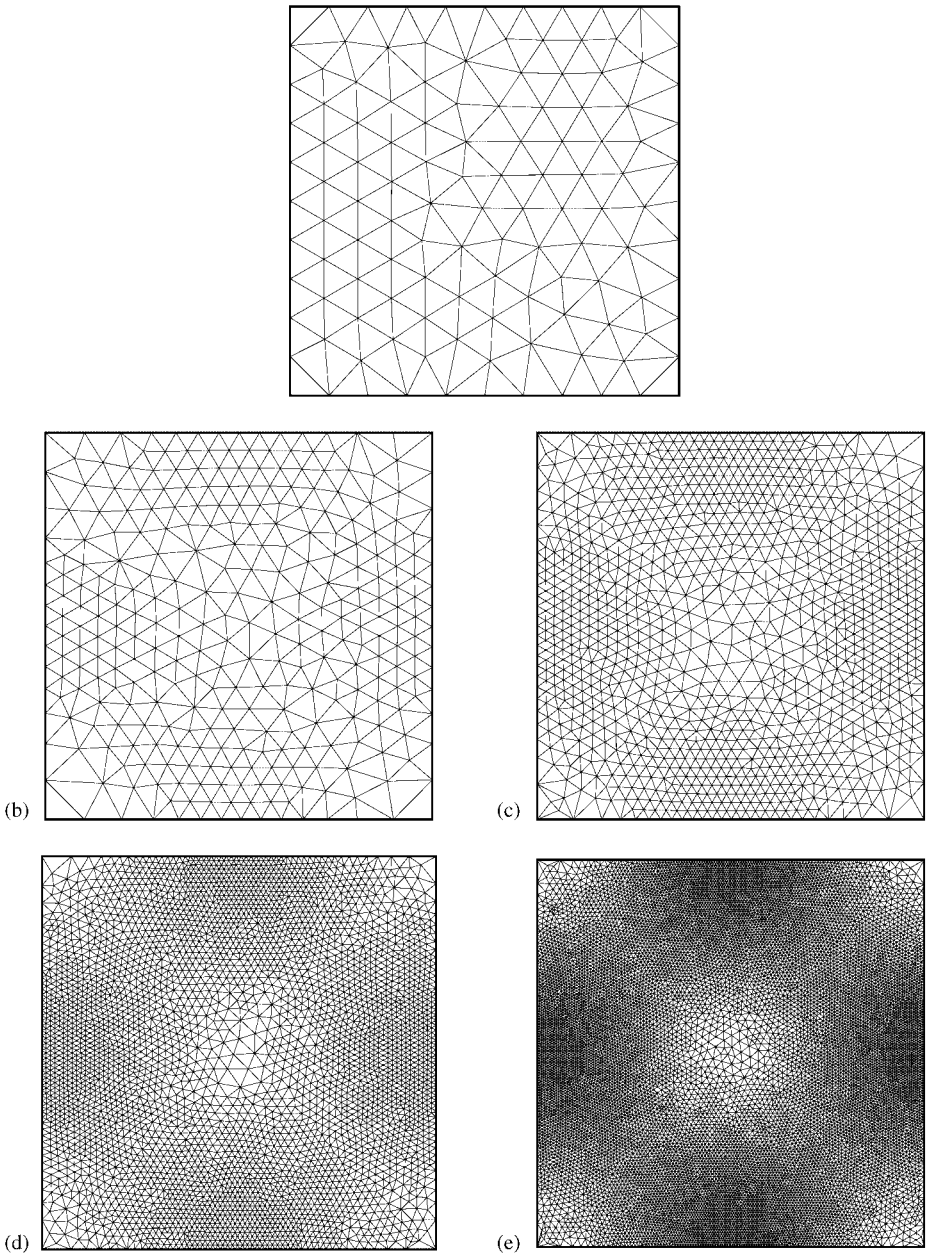

Figure 10. Adaptive grids at consequent steps: (a) initial grid; (b) 1st-adaptive grid; (c) 2nd-adaptive grid; (d) 3rd-adaptive grid; and (e) final adaptive grid.

reduced by half so that the relatively finer grid will be generated subsequently. As indicated in Figure 10(b)–(e), the cells in the regions with considerably large gradients are reasonably refined. In other words, the regions with large gradients, as highlighted in Figure 8(b), are successfully

DOI: 10.1002/fld

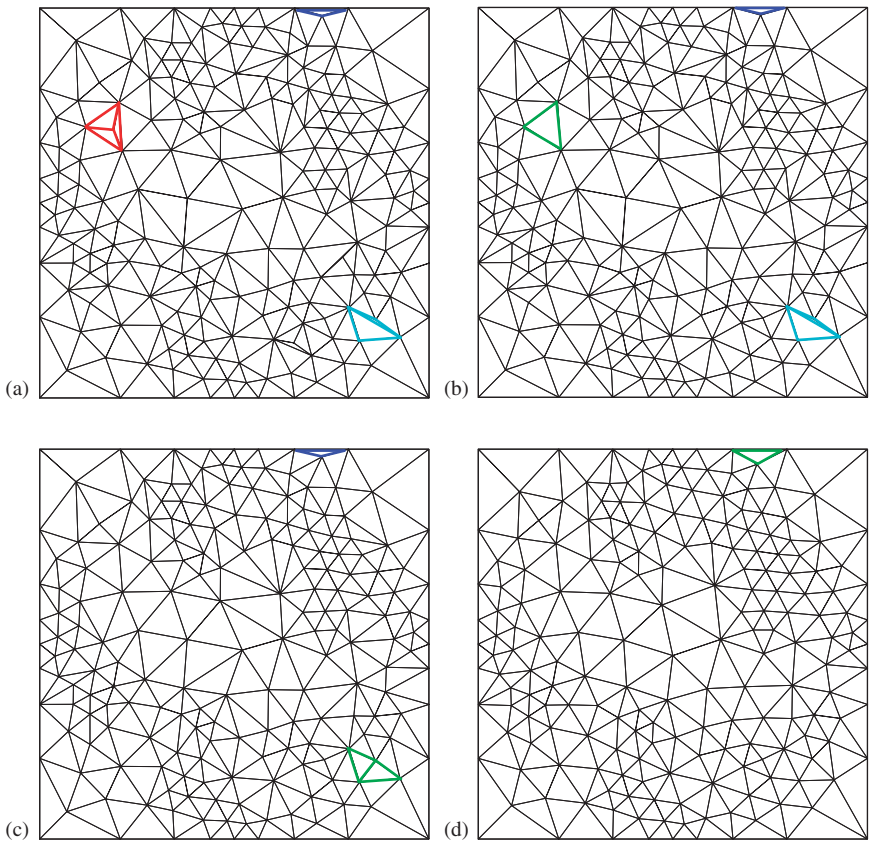

Figure 11. Comparison of adaptive grids without and with cosmetic treatment: (a) without cosmetic treatment; (b) with removal of triangles only; (c) with removal of triangles and diagonal swapping only; and (d) with removal of triangles, diagonal swapping and grid smoothing (cells in red, blue and cyan: selected cells with poor quality without cosmetic treatment; cells in green: cells after cosmetic treatment).

and accurately resolved with fine grid deployed by the adaptive remeshing technique adopted in the current study.

Some cosmetic techniques, including removal of redundant cells, diagonal swapping of cell-edges and grid smoothing, which are widely used in grid generation community for purposes to improve the grid quality, have also been adopted in the proposed adaptive remeshing procedure. The effects of these techniques are graphically illustrated in Figure 11. As shown in Figure 11(a), without any cosmetic treatment, there are some highly distorted cells occurring in the domain. They may result from the limited space for the last set of fronts during the domain triangulation by the advancing front method. As shown in Figure 11(b), the removal of redundant triangles cannot only reduce the number of nodes as well as cells, but improve the grid quality to some extents. Thanks to simply diagonal swapping treatment, some neighboring cells are reconstructed, which leads to substantial improvement in grid quality, as shown in Figure 11(c). In such a process, all nodes and the number of cells are remained invariant while the linkages for affected cells are

DOI: 10.1002/fld

Table I. Comparison of numerical errors for grids improved with cosmetic techniques.

Case no.	Cosmetic treatment	No. of nodes	Irregularity (γ)	L2-norm error
1.	No	196	0.07567	6.9575×10^{-3}
2.	Removal of triangles	193	0.07223	6.6400×10^{-3}
3.	Removal of triangles; diagonal swapping	193	0.06545	5.7165×10^{-3}
4.	Removal of triangles; diagonal swapping; grid smoothing	193	0.04590	5.5950×10^{-3}

Table II. Numerical errors of adaptive GSM solutions with cosmetic techniques.

Stage	No. of nodes	Averaged nodal spacing (h)	L2-norm error (error)	CPU time (s)	γ	$\delta_{\min}$	$\delta_{\max}$
Initial	123	9.91E−02	1.57E−02	5.30E−02	2.19E−02	1.00E−01	0.1
1st	304	6.08E−02	2.83E−03	2.14E−01	2.05E−02	5.00E−02	0.1
2nd	1099	3.11E−02	6.88E−04	2.92E+00	1.42E−02	2.50E−02	0.1
3rd	4014	1.60E−02	9.02E−05	5.07E+01	1.21E−02	1.25E−02	0.1
4th	15149	8.19E−03	4.45E−05	9.89E+02	9.90E−03	6.25E−03	0.1

Table III. Numerical errors of adaptive GSM solutions without cosmetic techniques.

Stage	No. of nodes	Averaged nodal spacing (h)	L2-norm error (error)	CPU time (s)	γ	$\delta_{\min}$	$\delta_{\max}$
Initial	123	9.91E−02	1.65E−02	5.30E−02	3.17E−02	1.00E−01	0.1
1st	309	6.03E−02	3.06E−03	6.90E−01	3.46E−02	5.00E−02	0.1
2nd	1121	3.08E−02	6.13E−04	3.93E+00	2.75E−02	2.50E−02	0.1
3rd	4027	1.60E−02	2.00E−04	5.17E+01	2.34E−02	1.25E−02	0.1
4th	15200	8.18E−03	9.36E−05	1.22E+03	2.09E−02	6.25E−03	0.1

changed only. Furthermore, as depicted in Figure 11(d), as each interior node is shifted towards the center of a polygon that is formed by all triangles linked with the node, the quality of overall set of grid is further improved. Such substantial enhancement can also be found in Table I in terms of number of nodes and irregularity of resultant grids.

Numerical errors of the adaptive GSM solutions obtained with and without the use of cosmetic techniques are summarized in Tables II and III, respectively. For comparison purpose, the numerical errors based on global refinement procedure are also tabulated in Table IV. As described in the preceding section about the adaptive procedure, the sets of adaptive grids are obtained by maintaining the value for $\delta_{\max}$ and halving the value for $\delta_{\min}$ consequently during the adaptive process. The evolution of computational errors of adaptive solutions to the Poisson equation can also be found in Figure 12.

As shown in Table II, as the adaptive process advances, the numerical error will decrease monotonically, as well as the grid irregularity. This confirms that the successful clustering of nodes

DOI: 10.1002/fld

Table IV. Numerical errors of GSM solutions based on global refinement.

Stage	No. of nodes	Averaged nodal spacing (h)	L2-norm error (error)	CPU time (s)	γ
Initial	123	9.91E−02	1.57E−02	5.30E−02	2.19E−02
1st	311	6.01E−02	6.24E−03	2.26E−01	1.28E−02
2nd	1104	3.10E−02	1.44E−03	1.96E+00	6.17E−03
3rd	4048	1.60E−02	3.73E−04	3.20E+01	3.10E−03
4th	15272	8.16E−03	9.43E−05	5.39E+02	2.09E−03

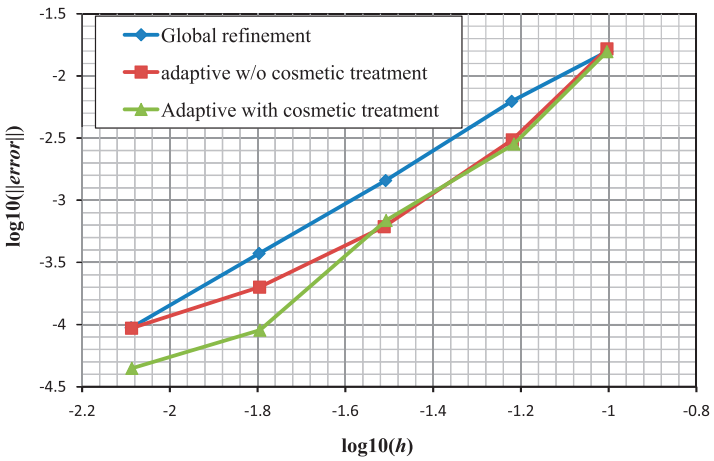

Figure 12. Evolution of computational errors with the changes in averaged cell spacing.

toward the regions with high gradients, thanks to the proposed adaptive procedure, gives rise to the remarkably improved accuracy, with comparison to cases with the same number of nodes uniformly distributed across the field. Once a relatively larger number of nodes are generated, it is necessary to embark the cosmetic techniques with the adaptive procedure to improve the grid quality so that the adaptive remeshing procedure still yields higher accuracy than the global refinement process. This can be seen by comparing the data in Tables II and III, and in Figure 12. Figure 12 also tells that the adaptive GSM can produce results at an expected accuracy with much less number of nodes than the GSM solutions based on global refinement. As shown in Tables II and IV, for an anticipated accuracy, it is allowed for a much less number of nodes using in the proposed adaptive remeshing procedure than in the global refinement procedure. This will result in dramatically reduced demand in computational cost, too.

It should be mentioned that the proposed GSM solver always gives accurate results for all sets of grids studied here, including those grids with highly distorted cells. Such a behavior again implies that the developed GSM should be very robust and stable, as already addressed by Liu and Xu [2]. Such an attractive feature will motivate us toward the development of anisotropic adaptive GSM in immediate future, where stable and accurate solutions are still anticipated but more irregular cells will have to be used.

DOI: 10.1002/fld

4.2. Solutions to Euler equations

4.2.1. Governing equations. In Cartesian coordinate system, without consideration of source terms, the two-dimensional Euler equations for inviscid compressible flows take the following form:

$$\frac{\partial \vec{W}}{\partial t} + \nabla \cdot \vec{F}_c = 0 \tag{39}$$

where $\vec{W}$ and $\vec{F}_c$ represent, respectively, the vectors of conservative variables, the convective fluxes. They are in the form of

$$\vec{W} = \begin{bmatrix} \rho \\ \rho u \\ \rho v \\ \rho E \end{bmatrix}, \quad \vec{F}_c = \begin{bmatrix} \rho V \\ \rho u V + n_x p \\ \rho v V + n_y p \\ \rho \left(E + \dfrac{p}{\rho} \right) V \end{bmatrix} \tag{40}$$

where ρ, u, v, p, and E denote the density, the two Cartesian velocity components, static pressure, and the total internal energy, respectively. The contravariant velocity is defined as

$$V = \vec{v} \cdot \vec{n} = n_x u + n_y v \tag{41}$$

To close the equations, the equation of state is also included:

$$p = \rho R T \tag{42}$$

where R is the gas constant and T is the temperature of the air.

The well-known second-order ROE method [24], which is based on the left and right states with the help of Barth and Jespersen scheme [25], is used to predict the convective fluxes. Venkatakrishnan's limiter [26] is employed to avoid unphysical oscillation in solutions. The explicit 5-stage Runge–Kutta method, as described previously, is used here for steady-state solutions.

4.2.2. Boundary conditions. The boundary control surfaces are used to close the smoothing domains at boundaries. At a corner point where two or more boundaries meet with each other, the boundary control surface is split into control surfaces for each boundary condition separately.

- *Solid wall*

In inviscid flows, slip wall conditions are imposed on the solid boundaries. As viscous friction is ignored, the velocity vector must be tangential to the surface. This implies that the normal velocity is zero. Hence, the contravariant velocity V is zero. Consequently, the vector of convective fluxes in the governing equation reduces the pressure terms alone. That is to say,

$$\vec{F}_c = \begin{bmatrix} 0 \\ n_x p_{\mathrm{w}} \\ n_y p_{\mathrm{w}} \\ 0 \end{bmatrix} \tag{43}$$

where p_{w} denotes the wall pressure.

- *Farfield*

DOI: 10.1002/fld

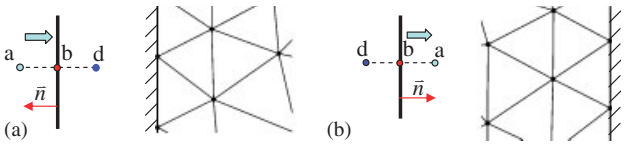

Figure 13. Definition of farfield boundaries: (a) subsonic inflow boundary and (b) subsonic outflow boundary.

The farfield conditions are imposed to the external bounds of the computational domains. As addressed in Blazek [15], the numerical implementation of the farfield conditions has to fulfill two basic requirements. First, the truncation of the domain should have no notable effects on the flow solution as compared with the infinite domain. Second, any outgoing perturbations must not be reflected back into the flow field. The farfield conditions based on the concept of characteristic variables are employed in the current study. For the cases of the subsonic or transonic flows that are studied here, the farfield conditions for subsonic inflow and outflow are applied to external bounds in the simulations.

For a subsonic inflow, as shown in Figure 13(a), the following formulations are imposed at the farfield bounds:

$$\begin{aligned} p_b &= \tfrac{1}{2}\{p_a + p_d - \rho_0 c_0[n_x(u_a - u_d) + n_y(v_a - v_d)]\} \\ \rho_b &= \rho_a + (p_a - p_d)/c_0^2 \\ u_b &= u_a - n_x(p_a - p_b)/(\rho_0 c_0) \\ v_b &= v_a - n_y(p_a - p_b)/(\rho_0 c_0) \end{aligned} \tag{44}$$

where ρ_0 and c_0 correspond to values at the reference state that is set equal to the state at the interior point. The values at point a are determined from the freestream state.

For a subsonic outflow as shown in Figure 13(b), the variables at farfield boundaries are obtained from

$$\begin{aligned} p_b &= p_a \\ \rho_b &= \rho_d + (p_b - p_d)/c_0^2 \\ u_b &= u_d + n_x(p_d - p_b)/(\rho_0 c_0) \\ v_b &= v_a + n_y(p_d - p_b)/(\rho_0 c_0) \end{aligned} \tag{45}$$

with p_a being the prescribed static pressure.

In the present study, one-layer of dummy cells is generated on the farfield boundaries, which is used to determine the values of field variables and their gradients on the boundaries. Besides, the vortex correction in 2D, suggested by Usab and Murman [27], is included in the calculation at the farfield boundaries in order to shrink the computational domain.

4.2.3. Adaptive GSM solutions. The adaptive GSM solver is used to solve the transonic inviscid flow over the NACA0012 airfoil. For the testing case, the freestream corresponds to the following conditions: $T_\infty = 288\,\mathrm{K}$, $p_\infty = 1.0 \times 10^5\,\mathrm{Pa}$, $Ma = 0.8$, and $\alpha = 1.25$. Here, T_∞, p_∞, and Ma denote, respectively, the temperature, static pressure, and Mach number of the freestream, and α stands

DOI: 10.1002/fld

for the angle of attack of the NACA0012 airfoil. In this test case, a strong shock occurs on the upper surface of the airfoil and another relatively weak shock takes place on the lower surface.

As shown in Figure 14(a), based on a set of relatively coarse grid, both the shocks are captured in the standard GSM solver. However, it is obvious that the two predicated shocks are pretty wide, which can be attributed to the insufficient resolution of grid near the shock regions. The proposed adaptive GSM solver described in the preceding sections is used to improve the resolutions in both the shock regions. In this study, error indicators based on the first and second derivatives of density, respectively, are tested for comparison and the GSM results for the two options are presented in details below.

As reported in the section about GSM solutions to the Poisson equation, the error indicators based on first derivatives are sufficiently good to identify the regions to be refined, which correspond to relatively large gradients in the smooth flow field. Since the first derivatives of density are necessarily approximated and stored in the GSM analyses of the inviscid flow over the NACA 0012 airfoil, it is intrinsic to re-use them to estimate error indicators in the adaptive GSM solver. The consequent adaptive grids and solutions are shown in Figure 14(a)–(e). It is striking that the grids around the strong shock are sufficiently refined and the predicted shock front becomes thinner as expected. However, it should be noted that the grid resolution around the weak shock is not improved. The similar observation has ever been reported by Giraldo FX [19].

Besides, studies about this option also reveal that the final adaptive results show high dependence on the resolution of boundary nodes on the airfoil surfaces. It should be mentioned that the results shown in Figure 14 have been obtained with the help of additional constraint for preserving the shape of the airfoil with sufficient enough boundary nodes. When a set of considerably coarse grid, as shown in Figure 17(a), is used as the initial grid and the boundary nodes on the wall surfaces are allowed to be freely adapted with the algorithm described in the preceding section, subsequent adaptive grids, as shown in Figure 15, are found to fail in accurately resolving the leading edge and thus the predicted strong shock is wrongly pushed towards the trailing edge. The manifest deviation can also be seen in Figure 16 where the pressure coefficients on the airfoil surfaces are plotted. In summary, the two scenarios are considered here: In the free adaption scenario, the boundary nodes on the wall surfaces are purely adapted according to the estimated errors based on local first derivatives of density. In the second scenario, a minimum grid size is imposed such that the shape of the wall geometry can be well preserved during the adaptive process. It is noticeable that the strong shock occurring on the upper surface is always successfully captured and resolved with finer grids in both the scenarios. While, the weak shock on the lower surface can be visible only in the second scenario where the nodes distributed on the wall are manipulated so as to accurately preserve the physical shape of the airfoils.

Alternatively, the error indicators based on the second derivatives of density, as described in Equation (25), are also examined in this case. With this option, a set of considerably coarse grid (see Figure 17(a)) is used as the initial grid and the nodes on the airfoil surfaces are freely adapted. The adaptive grids as well as the corresponding GSM solutions are shown in Figure 17. In comparison with error indictors using first derivatives of density, relatively broader zones are identified for further refinement in the very first adaptive process, as shown in Figure 17(b). The shock front is not sufficiently refined, but its adjacent regions are refined instead. As shown in Figure 17(c)–(e), as the adaption progresses, the narrower regions across the shocks are successively refined and thus the shock front is necessarily refined, too. We find out that the multiple key features in the transonic flow over the NACA0012 airfoil, which occur at the two shock regions, the leading, and

DOI: 10.1002/fld

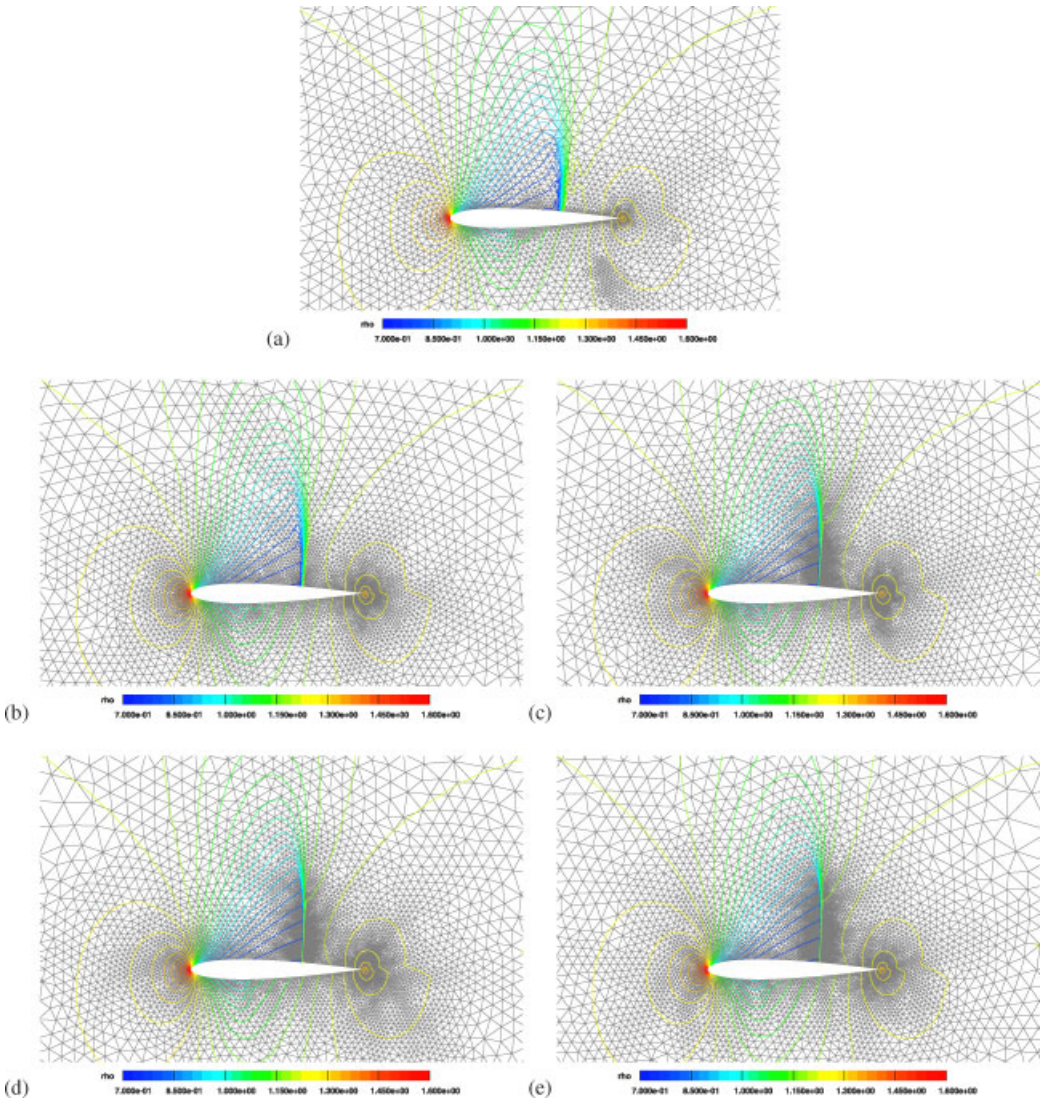

Figure 14. Plots of adaptive grids and contours of density obtained with the adaptive GSM solver based on the first-derivatives of density: (a) initial grid (boundary preserving, $n_{\text{node}} = 8346$); (b) 1st-adaptive grid ($n_{\text{node}} = 9381$); (c) 2nd-adaptive grid ($n_{\text{node}} = 12\,788$); (d) 3rd-adaptive grid ($n_{\text{node}} = 14\,139$); and (e) final adaptive grid ($n_{\text{node}} = 17\,955$).

trailing edges, respectively, are all well resolved in the adaptive analyses. In addition, the nodes distributed on the wall surfaces are freely and necessarily refined so that the shape of the wall geometries is well captured. In summary, the option for error indicators based on second derivatives is more accurate to capture all the key features than the option based on first derivatives.

DOI: 10.1002/fld

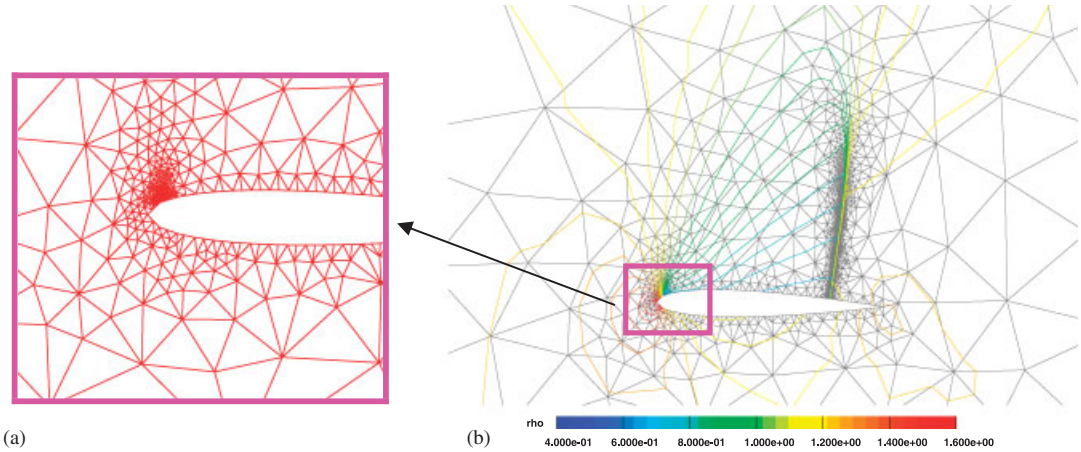

Figure 15. Effects of resolutions of initial meshes on the accuracy of adaptive solutions: (a) close-up view of poor grid resolution at the leading edge and (b) global view of the adaptive grid and contour plot of density.

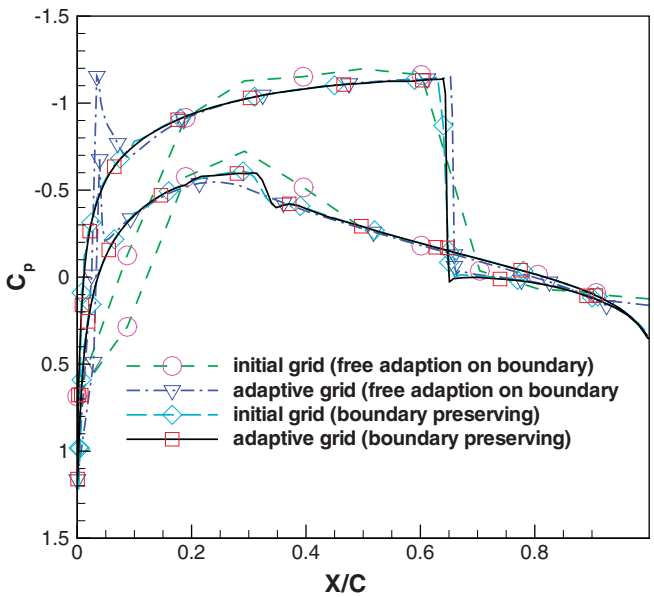

Figure 16. Predicted pressure coefficients with the adaptive GSM solver based on first derivatives of density.

Figure 18 shows the predicted pressure coefficients on the surface of the airfoil for both the options tested in the current study. Apparently, based on the second derivatives of density, the weak-shock region is precisely resolved as well as the strong shock region, leading edge and

DOI: 10.1002/fld

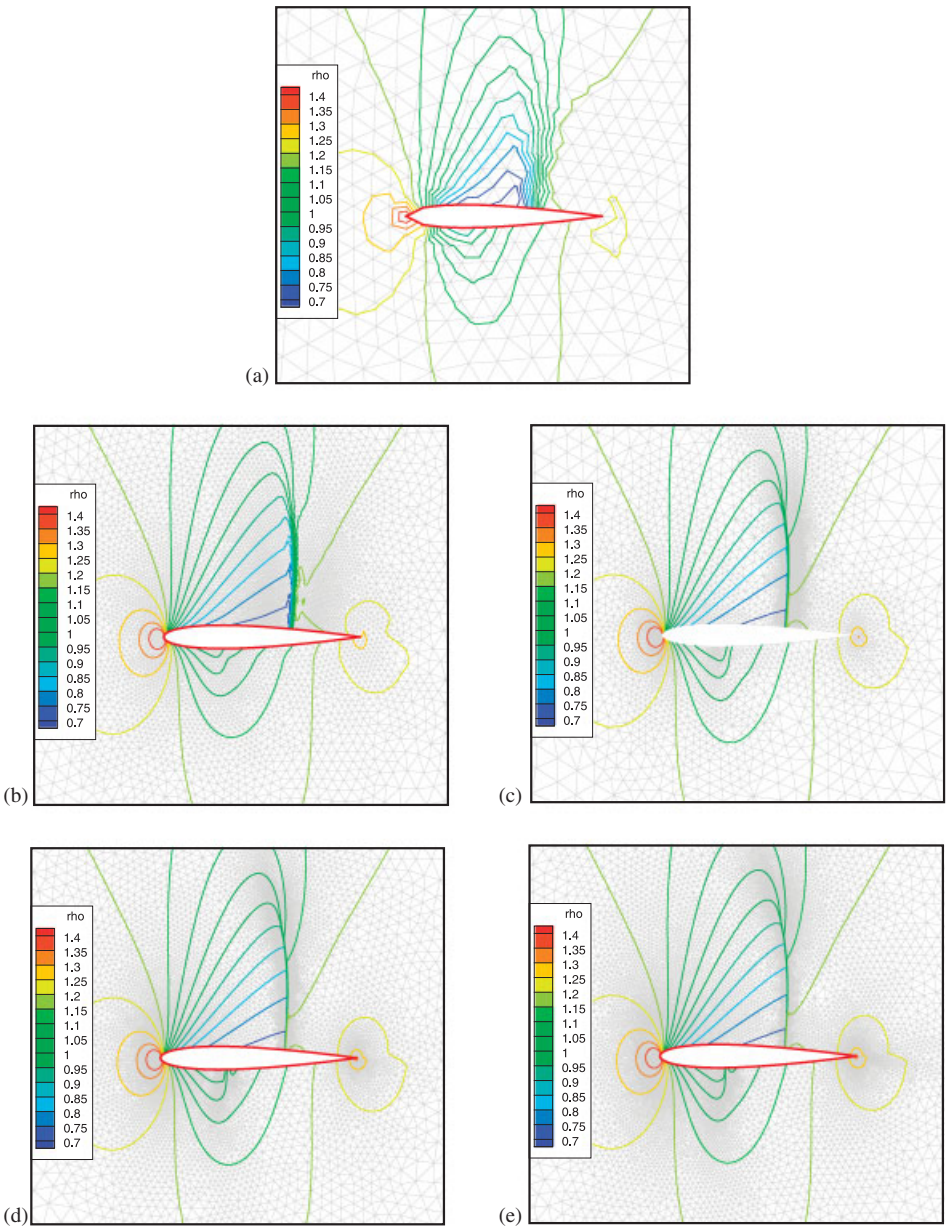

Figure 17. Plots of adaptive grids and contours of density obtained with the adaptive GSM solver based on the second derivatives of density: (a) initial grid (free adaption on boundaries, $n_{\text{node}} = 3927$); (b) 1st-adaptive grid ($n_{\text{node}} = 8718$); (c) 2nd-adaptive grid ($n_{\text{node}} = 10\,148$); (d) 3rd-adaptive grid ($n_{\text{node}} = 25\,665$); (e) final adaptive grid ($n_{\text{node}} = 34\,079$).

DOI: 10.1002/fld

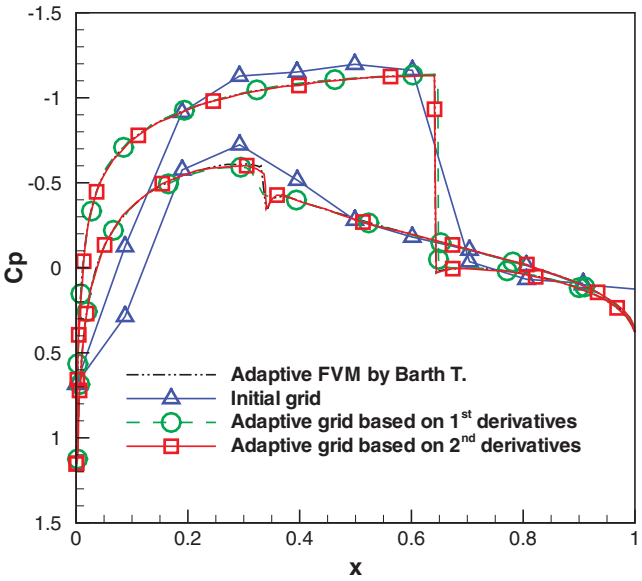

Figure 18. Predicted pressure coefficients with the adaptive GSM solver.

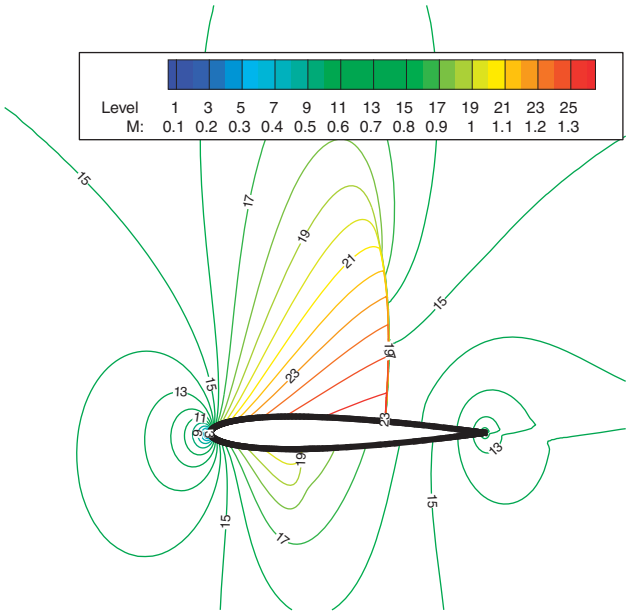

Figure 19. Contour plot of the Mach number using the final adaptive grid based on the second derivatives of density.

DOI: 10.1002/fld

trailing edge. Our results are agreeable well with Barth's analysis [28] which is obtained based on unstructured finite volume method.

The contour plot of the Mach number obtained in the adaptive GSM procedure with the second option is shown in Figure 19. It is clear that the both shocks, as well as the stagnation point on the leading edge and wake flow near the trailing edge are well solved.

Ideally, the proposed adaptive procedure is anticipated to be able to automatically identify most key features that are required to be refined. The first option based on first derivatives of density has been proved to be the ideal candidate for smooth flow fields. In flows with discontinuities, it also effectively and successfully resolves the dominant shock, but fails in capturing some other key features which concurrently occur in the flows but in relatively weaker strengths. The main reason for such a failure is that the fist-derivative-based error indicator cannot resolve the boundary correctly. Comparatively, the second option based on second derivatives of density leads to the expected adaptive grid to resolve all the key features, as well as the boundary shape, in the flows with discontinuities. The merit in accuracy may be due to the consistency in the order of accuracy adopted in both the error indicator and the GSM solver. This may be considerably important for the accurate resolution of boundary nodes. Thus, for flows with multiple key features with different strengths, it is more preferable to use the second derivatives for estimating the error indicators in the adaptive GSM procedure.

5. CONCLUSION

In the current study, a novel gradient smoothing method (GSM) formulated based on the strong form of governing equations is developed with adaptive remeshing technique based on the advancing front method. The GSM solver is valid for both regular and irregular cells so that flow behaviors with domains of arbitrary geometry can be easily resolved. With the inclusion of adaptive remeshing technique, the flows involving discontinuity or abrupt changes in space, such as a shock flow, can be more precisely simulated. It is found that

- The proposed GSM scheme is very robust and stable so that it consistently results in accurate results even for a set of grid with highly distorted cells.
- The adaptive GSM provides more accurate solutions, thanks to the 'optimal' grid achieved with the error equidistribution strategy. On the other hand, the adaptive GSM can yield as accurate results as the non-adaptive GSM but with remarkably less number of nodes.
- The proposed adaptive GSM is very stable during the overall adaptive process. As a large number of nodes is generated in the domain, it is found that the cosmetic techniques can effectively improve the grid quality and correspondingly the benefits from the adaptive solver can be continuously possessed.
- The first-derivative-based error indicator is good enough to resolve the smooth flow field and the dominant shock in the discontinuous flows. However, care should be taken to enforce the boundary nodes to well represent the shape of the boundary geometry.
- As the second-derivative-based error indicator is used, all key flow features in the shock flow fields, as well as the shape of wall boundaries, can be effectively and automatically identified and then resolved accordingly. Thus, for abruptly changed flows with multiple key features, it is recommended to use the second derivatives of density for error indicators estimation in the proposed adaptive GSM solver.

DOI: 10.1002/fld

ACKNOWLEDGEMENTS

The authors gratefully acknowledge the invaluable comments and guidelines given by Prof. N. P. Weatherill from University of Swansea during his visit in the Institute Of High Performance Computing, Singapore. Thanks will also be extended to Dr Alex Lee for his generous help and support.

REFERENCES

1. Hoffmann JD. *Numerical Methods for Engineers and Scientists* (2nd edn). Engineering Education System^{TM}, Marcel Dekker, Inc: New York, Basel, 2001.
2. Liu GR, Xu GX. A gradient smoothing method (gsm) for fluid dynamics problems. *The International Journal for Numerical Methods in Fluids* 2008; **58**:1101–1133.
3. Chen JS, Wu CT, Yoon S, You Y. A stabilized conforming nodal integration for Galerkin grid-free methods. *International Journal for Numerical Methods in Engineering* 2001; **50**:435–466.
4. Liu GR, Zhang GY, Dai KY, Wang YY, Zhong ZH, Li GY, Han X. A linearly conforming point interpolation method (LC-PIM) for 2D solid mechanics problems. *International Journal of Computational Methods* 2005; **2**(4):645–665.
5. Zhang GY, Liu GR, Wang YY, Huang HT, Zhong ZH, Li GY, Han X. A linearly conforming point interpolation method (LC-PIM) for three-dimensional elasticity problems. *International Journal for Numerical Methods in Engineering* 2007; **72**:1524–1543.
6. Lucy L. A numerical approach to testing the fission hypothesis. *The Astronomical Journal* 1977; **82**:1013–1024.
7. Liu GR, Liu MB. *Smoothing Particle Hydrodynamics—A Meshfree Particle Method*. World Scientific Publishing: Singapore, 2003.
8. Peraire J, Vahdati M, Morgan K, Zienkiewics OC. Adaptive remeshing for compressible flow computations. *Journal of Computational Physics* 1987; **72**:449–466.
9. Knabner P, Angermann L. *Numerical Methods for Elliptic and Parabolic Partial Differential Equations*. Springer: Berlin, 2003.
10. Eringen AC, Edelen DGB. On nonlocal elasticity. *International Journal of Engineering Science* 1972; **10**:233–248.
11. Chen JS, Yoon S, Wu CT. Non-linear version of stabilized conforming nodal integration for Galerkin grid-free methods. *International Journal for Numerical Methods in Engineering* 2002; **53**:2587–2615.
12. Liu GR, Li Y, Dai KY, Luan MT, Xue W. A linearly conforming radial point interpolation method for solid mechanics. *International Journal of Computational Methods* 2006; **3**:401–428.
13. Liu GR, Dai KY, Nguyen TT. A smoothed finite element method for mechanics problems. *Computational Mechanics* 2007; **39**:859–877.
14. Liu GR, Nguyen TT, Dai KY, Lam KY. Theoretical aspects of the smoothed finite element method (SFEM). *International Journal for Numerical Methods in Engineering* 2007; **71**:902–930.
15. Blazek J. *Computational Fluid Dynamics*: *Principles and Application* (1st edn). Elsevier Press: Oxford, 2001.
16. Moinier P. Algorithm developments for an unstructured viscous flow solver. *Ph.D. Thesis*, University of Oxford, 1999.
17. Babuska I, Rheinboldt W. Error estimates for adaptive finite element computations. *SIAM Journal on Numerical Analysis* 1978; **15**:736–754.
18. Peiro J, Peraire J, Morgan K. FELISA SYSTEM Version 1.1—Reference Manual, 1994.
19. Giraldo FX. A space marching adaptive remeshing technique applied to the 3D Euler equations for supersonic flow. *Ph.D. Thesis*, University of Virginia, 1995.
20. Thompson JF, Soni BK, Weatherill NP. *Handbook of Grid Generation*. CRC Press: Boca Raton, 1999.
21. Lohner R. *Applied Computational Fluid Dynamics Techniques*: *An Introduction Based on Finite Element Methods*. Wiley: New York, 2001.
22. Stillinger DK, Stillinger FH, Torquato S, Truskett TM, Debenedetti PG. Triangle distribution and equation of state for classical rigid disks. *Journal of Statistical Physics* 2000; **100**(1–2):49–71.
23. Liu GR. *Grid Free Methods*: *Moving beyond the Finite Element Method*. CRC Press: Boca Raton, 2002.
24. Roe PL. Approximate Riemann solvers, parameter vectors, and difference schemes. *Journal of Computational Physics* 1981; **43**:357–382.
25. Barth TJ, Jespersen DC. The design and application of upwind schemes on unstructured grids. *AIAA Paper 89-0366*, 1989.

DOI: 10.1002/fld

26. Venkatakrishnan V. Convergence to steady-state solutions of the Euler equations on unstructured grids with limiters. *Journal of Computational Physics* 1995; **118**:120–130.
27. Usab WJ, Murman EM. Embedded mesh solution of the Euler equation using a multiple-grid method. *AIAA Paper 83-1946*, 1983.
28. Barth TJ. *Aspects of Unstructured Grids and Finite-volume Solvers for the Euler and Navier–Stokes Equations*. VKI Lecture Series in CFD course 1994. Von Karman Institute: Belgium, 1994.

DOI: 10.1002/fld